Beam-on-Foundation Modelling and Closed Loop Control of Tool to Tissue Interaction for Percutaneous Needle Steering

Timothy Adejare Ayelagbe
Department of Electronic and Electrical Engineering
Obafemi Awolowo University
Ile-Ife, Nigeria
timothyayelagbe@gmail.com

***Abstract*—This paper presents a MATLAB simulated pipeline for robot assisted bevel tipped needle steering, aimed at applications such as biopsy, brachytherapy, and targeted drug delivery. It combines four established parts into one closed feedback loop: an assumed modes Euler-Bernoulli beam on a Winkler elastic-foundation, a nonholonomic bicycle kinematic model, duty cycle bevel steering, and a pole placement PID controller with a saturation-aware integral rule. None of these four parts is new on its own. The contribution is how they are wired together: the beam model and the kinematic controller are usually studied separately, and here a single explicit coupling rule lets the mechanics sub-model actually drive the real time curvature command, via one calibration constant that converts a beam-computed tip slope into a curvature. We show that this exposes something a disconnected simulation would not: the effective plant gain changes with insertion depth, which a fixed-gain PID controller cannot correct for, producing a threefold drop in weak regulation accuracy. Since the calibration constant is set from one reference condition rather than fitted to data, we run a sensitivity check showing which conclusions survive if its true value differs, and which do not. We also include a Rayleigh-Ritz mode count convergence study and a two dimensional sweep of controller bandwidth against reference frequency, revealing a tracking error surface that rises and falls rather than trading off smoothly.**

***Index Terms*—Needle steering, beam-on-elastic foundation, Rayleigh-Ritz method, nonholonomic kinematics, duty-cycle steering, PID control, percutaneous surgery.**

I. Introduction

Percutaneous needle insertion is the basis of biopsy, brachytherapy, regional anaesthesia, and localized drug delivery. A bevel tipped needle has a cutting edge that is angled rather than flat, so the tissue pushes back unevenly on the tip as the needle goes in, and the needle bends and curves instead of moving in a straight line. Left uncorrected, this can mean a poorly sampled biopsy, a nerve block that misses its target, or radiation delivered to the wrong spot. Robot assisted steering addresses this by combining three things: (i) a model that predicts deflection, (ii) a steering strategy, most commonly spinning the bevel on and off in a duty cycle, and (iii) a feedback controller that watches the tip and corrects it. Each of these three pieces is well studied on its own. This paper is about what happens when they are wired together into one working pipeline, and, in particular, what new problems show up only once they are actually connected.

Contribution. This paper does not introduce a new deflection mechanism, steering strategy, or control law. All four building blocks, the Rayleigh-Ritz beam-on-foundation model, nonholonomic bicycle kinematics, duty-cycle bevel steering, and pole-placement PID control, come from established prior work, reimplemented from first principles. The contribution is the integration: (1) reimplementing the Webster-Misra-Roesthuis-Minhas pipeline in MATLAB, checking every sub-model against a known limiting case, including a mode-count convergence study; (2) a pole-placement PID controller respecting the double-integrator structure of the linearized bicycle model, with a saturation-aware integral rule; (3), the central contribution, an explicit coupling rule connecting the beam-mechanics sub-model to the real-time curvature command through one calibration constant, so the mechanics genuinely drives the control loop rather than sitting beside it; and (4) using this coupling, with a sensitivity check on the calibration constant, to quantify something a disconnected version would not reveal: the plant gain changes with insertion depth, degrading fixed-gain weak regulation by about a factor of three. We also sweep controller bandwidth against reference frequency and show tracking error does not simply trade off with bandwidth.

Section II reviews related work. Section III describes the architecture. Section IV derives each sub-model and the coupling law. Section V presents results. Section VI discusses limitations and next steps. Section VII concludes.

II. Related Work

Webster et al. [1] introduced the nonholonomic bicycle-model description of bevel-tipped needle steering, treating the needle tip like a vehicle that can only move forward and turn, never slide sideways. Misra et al. [2] and Roesthuis et al. [3] instead derived needle deflection from mechanics, modelling the needle shaft as an Euler-Bernoulli beam resting on a Winkler foundation and solving it with the Rayleigh-Ritz method. Minhas et al. [4] introduced duty-cycled bevel rotation, where the bevel is flipped back and forth to average out the curvature; this bevel-flipping approach is used in Section IV-D. The mode-shape eigenvalues used throughout follow Blevins [5], and the needle and tissue parameters in Table II come from Roesthuis et al. [3].

Coupling a mechanics-based deflection model into a real-time controller is not, by itself, a new idea. Roesthuis, Abayazid, and Misra [7] extended the beam-on-foundation description to multi-bend insertion inside a control loop; Khadem et al. [8] built a real-time mechanics-based model driving a nonlinear model-predictive controller; and Adebar et al. [9] closed a full 3-D, ultrasound-guided loop around a mechanics-based deflection predictor. What sets this pipeline apart is not the closing of the loop itself but a specific, calibrated coupling between the Rayleigh-Ritz formulation and the duty-cycle kinematic controller of [1], [4], together with a quantitative, sensitivity-checked account of what this coupling costs a fixed-gain controller (Sections IV-E, V, VI).

On the experimental side, Zandonà et al. [10] compared the unicycle and extended-bicycle kinematic models against real needle-tip trajectories in transparent silicone prostate phantoms, tracked with an RGB-D camera and semantic segmentation, and found the simpler unicycle model consistently more accurate. Lehocky et al. [11] built a finite-element model of needle-brain tissue interaction with a hyperelastic, viscoelastic constitutive law, identifying needle-tip fillet radius and insertion speed as the dominant factors controlling tissue stress and strain. Neither work closes a real-time control loop around a mechanics-based deflection model, the gap this paper's coupling law addresses; both point to low-cost ways of grounding the calibration constant and tissue parameters used here in real data (Section VI).

III. System Architecture

The architecture in Fig. 1 has six functional blocks arranged in a single loop. A trajectory planner supplies the reference lateral position y_{ref}; the tracking error $e = y_{ref} - y_{meas}$ drives a PID controller whose output is shifted by $\frac{1}{2}$ and saturated to a duty cycle $DC \in [0, 1]$; the robot spins the needle according to a periodic bevel-orientation waveform; the needle-tissue system deflects according to the resulting effective curvature; and a sensor, such as ultrasound or MRI, closes the loop by measuring the tip position. Unlike a purely kinematic formulation, the effective curvature here comes from actually solving the beam-on-foundation equilibrium at the current insertion depth (Section IV-E), so the mechanics sub-model of Section IV-B genuinely drives the control loop rather than being checked for correctness on the side.

IV. Mathematical Formulation

A. Cantilever Mode Shapes

The needle shaft is modelled as a clamped-free Euler-Bernoulli beam. Any shape the beam can take is written as a weighted sum of mode shapes $M_i(z)$, which are used purely

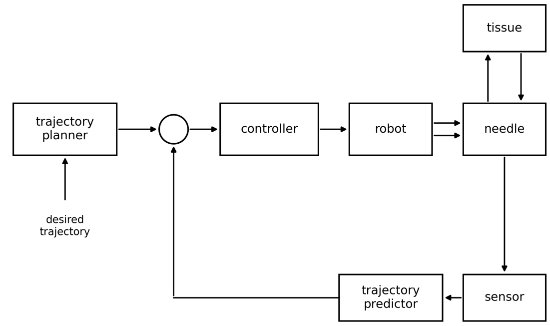

Fig. 1. Closed-loop architecture. The beam-coupled curvature law of Section IV-E is what makes the needle-tissue mechanics an active part of this loop rather than a parallel, unconnected sub-model.

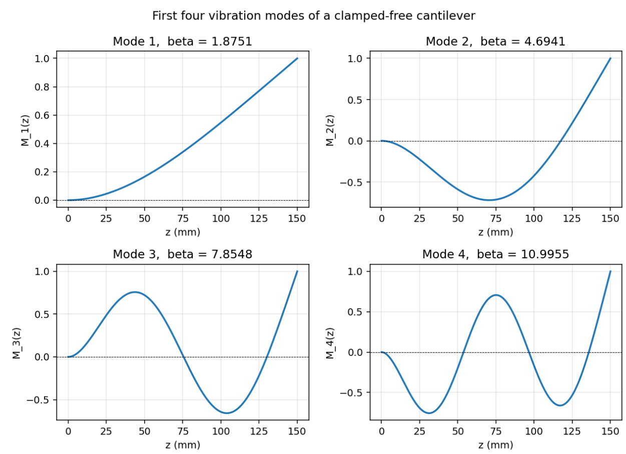

Fig. 2. First four assumed-mode shapes; the clamped-base condition is satisfied to 10^{-15}, and each mode is normalised so that $M_i(L) = 1$.

as spatial basis functions and satisfy the boundary conditions $M_i(0) = M_i'(0) = 0$ and $M_i''(L) = M_i'''(L) = 0$:

$$M_i(z) = \frac{1}{K_i}\Big[\sin(\beta_i z/L) - \sinh(\beta_i z/L) \\ - \gamma_i\big(\cos(\beta_i z/L) - \cosh(\beta_i z/L)\big)\Big] \quad (1)$$

where β_i solves

$$\cos\beta\cosh\beta = -1, \quad (2)$$

$$\gamma_i = \frac{\sin\beta_i + \sinh\beta_i}{\cos\beta_i + \cosh\beta_i}, \quad (3)$$

and K_i normalizes each mode so that $M_i(L) = 1$. The first four eigenvalues, taken from Blevins [5], are $\beta_1 = 1.8751$, $\beta_2 = 4.6941$, $\beta_3 = 7.8548$, $\beta_4 = 10.9955$ (Fig. 2).

Modal convergence. Table I extends N up to 6, using $\beta_5 = 14.1372$ and $\beta_6 = 17.2788$, and checks convergence at the deepest depth simulated, $d = L$. Throughout the rest of the paper we use $N = 4$, since this is already within 1.7% of the $N = 6$ result and adding more modes gives diminishing returns for a lot of extra computation.

TABLE I
MODAL CONVERGENCE OF TIP DEFLECTION $v(L)$ AT $d = 150$ MM

N	$v(L)$ (μm)	Δ from $N = 6$ (%)
1	263.4	49.7
2	442.4	15.5
3	497.5	5.0
4	514.4	1.7
5	520.8	0.55
6	523.8	–

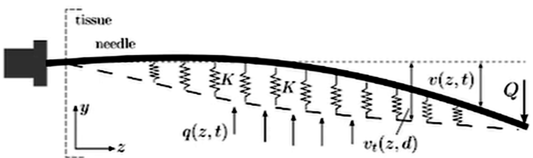

Fig. 3. Cantilever beam-on-elastic-foundation model of the needle shaft inside tissue. The inserted length is supported by a bed of springs of stiffness K, carrying a distributed reaction load $q(z,t)$ against the local tissue displacement $v_t(z,d)$, with tip force Q producing shaft deflection $v(z,t)$.

B. Beam-on-Elastic-Foundation Deflection

Fig. 3 shows the physical picture: the shaft is clamped at the actuator end, free at the tip, and the inserted length is pushed back by tissue modelled as a bed of independent springs. For a beam of flexural rigidity EI, classical Euler-Bernoulli beam theory [6] gives the governing equation

$$\frac{d^2}{dz^2}\left(EI\frac{d^2 v(z,t)}{dz^2}\right) = q(z,t), \tag{4}$$

where integrating $q(z,t)$ once gives the shear force (with Q entering as a boundary load), twice the bending moment, three times the deflection slope, and four times the deflection $v(z,t)$ itself.

Following [2], [3], the inserted length $[L-d, L]$ is supported by lateral springs of stiffness K_e, so $q(z,t) = K_e v(z,t)$. Integrating (4) directly is awkward here since the foundation region $[L-d, L]$ changes at every insertion step, so instead the shaft shape is written as a modal expansion, $v(z,d) = \sum_{i=1}^{N} M_i(z) g_i(d)$, and equilibrium is found by minimising the total potential energy $\Pi(d) = U_b + U_t + V$, where

$$U_b = \frac{EI}{2}\int_0^L (v'')^2\,dz, \tag{5}$$

$$U_t = \frac{K_e}{2}\int_{L-d}^{L} v^2\,dz, \tag{6}$$

$$V = -Q\,v(d,L), \tag{7}$$

which gives the linear system $\mathbf{A}\mathbf{g} = \mathbf{b}$,

$$\mathbf{A} = EI\,\mathbf{\Phi} + K_e\,\mathbf{\Lambda}, \qquad b_j = Q\,M_j(L), \tag{8}$$

with $\Phi_{ji} = \int_0^L M_i'' M_j''\,dz$, which does not change with depth, and $\Lambda_{ji}(d) = \int_{L-d}^{L} M_i M_j\,dz$, which is recomputed at every depth since its integration limits change with d.

TABLE II
NEEDLE AND TISSUE PARAMETERS (AFTER [3])

Parameter	Symbol	Value	Source
Young's modulus	E	200×10^9 N/m^2	[3]
Diameter	D	1.0–1.27 mm	[3]
Length	L	130–150 mm	[3]
Foundation stiffness	K_e	5.0×10^4 N/m^2	this work
Tip force	Q	0.5 N	this work

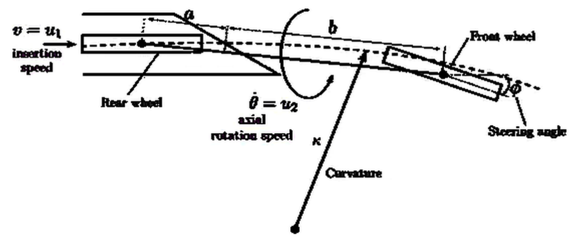

Fig. 4. Nonholonomic bicycle-model representation of the needle tip: insertion speed u_1, steering angle ϕ, and resulting curvature κ, following [1].

C. Nonholonomic Kinematic Model

For fast, real-time trajectory generation, the needle tip is treated as a nonholonomic bicycle-type vehicle [1] (Fig. 4), moving forward at speed $u_1 = \dot{d}$ with heading θ and effective curvature κ_{eff}:

$$\dot{x} = u_1 \cos\theta, \quad \dot{y} = u_1 \sin\theta, \quad \dot{\theta} = u_1 \kappa_{eff}. \tag{9}$$

In the purely kinematic version of the model, κ_{eff} is just a fixed number, the natural curvature $\kappa = \tan\phi/(a+b)$, set by the needle's bevel angle and geometry. Fig. 6 confirms that, as expected, a larger κ produces more lateral drift when $\kappa_{eff} = \kappa$ is held constant.

D. Duty-Cycle Curvature Steering

The bevel is flipped 180° for a fraction $DC \in [0,1]$ of each short period T, where T is much shorter than the total insertion time [4]. Averaging over one period gives the effective curvature

$$\kappa_{eff} = \kappa(1 - 2\,DC), \tag{10}$$

with the three anchor cases $DC = 0 \Rightarrow +\kappa$, $DC = 0.5 \Rightarrow 0$, and $DC = 1 \Rightarrow -\kappa$, all confirmed numerically (Fig. 7).

E. Beam-Coupled Curvature Law

Equation (10) makes κ_{eff} depend only on the duty cycle, with no connection to the beam mechanics of Section IV-B. This is the point where the mechanics model of Section IV-B and the kinematic steering law of Section IV-D are joined into a single coupling rule.

Coupling law. The duty-cycled bevel produces a direction-averaged transverse tip force, obtained using the same averaging argument as before:

$$Q_{eff}(t) = Q_{nom}\big(1 - 2\,DC(t)\big), \tag{11}$$

TABLE III
BEAM-COUPLED CURVATURE $\kappa_{beam}(d)$ AT $DC = 0$

d (mm)	κ_{beam} (m^{-1})	d (mm)	κ_{beam} (m^{-1})
5	1.647	75	1.023
10	1.051	100	1.005
20	0.901	125	1.000
30	0.969	150	1.000
50	1.052		

which reproduces the same three anchor cases as (10). At depth $d(t) = \min(u_1 t, L)$, solving $\mathbf{A}(d)\mathbf{g} = \mathbf{b}(Q_{eff})$ gives the tip slope

$$s(t) = v'(L, d(t)) = \sum_i g_i(t)\, M_i'(L), \tag{12}$$

which is used as the curvature indicator, since the bending curvature $v''(L)$ is always zero at a free tip and so cannot be used directly. A single calibration constant converts this slope into a curvature:

$$\kappa_{beam}(d, Q_{eff}) = C\, s(t), \quad C = \kappa / v'(L, L, Q_{nom}) = 81.66, \tag{13}$$

chosen so that full engagement under the maximum tip force ($d = L$, $DC = 0$) reproduces the same nominal curvature, $\kappa = 1.0$ m^{-1}, used in Section IV-C.

What this is, and is not. C is a single number chosen at one reference condition, not fitted to data or derived from first principles. Section IV-E is meant to demonstrate the coupling mechanism, namely that mechanics implies a plant gain that changes with depth, not to make a quantitative clinical prediction. To check how much this matters, Mode A and Mode B (Section IV-F) were rerun with C scaled up and down by $\sqrt{10}$. Mode B, the tracking case, stayed within 20% of its nominal result (12.0–14.7 mm RMS error) across the whole range, because the S-curve reference mostly covers depths where $\kappa_{beam}(d)$ has already settled (Table III). Mode A, the weak-regulation case, is far more sensitive: final error ranges from -31.7 mm at $C/\sqrt{10}$, through $+5.9$ mm at nominal C, to -0.5 mm at $C\sqrt{10}$, even changing sign along the way. The qualitative finding, that a fixed-gain controller tuned at one constant κ is mismatched to a plant whose gain changes with depth, holds across this whole range; the exact size of the Mode A error does not, and should not be read as a clinical prediction. Finding the true value of C from real data is a necessary first step before any such claim could be made (Section VI).

Depth-dependence. Table III reports $\kappa_{beam}(d)$ at $DC = 0$. Near the surface it overshoots the nominal value by 65%, dips about 10% below nominal near $d \approx 20$ mm, and settles beyond $d \approx 100$ mm, because the beam is more flexible, and so more sensitive to the tip force, when less of it is engaged by the surrounding tissue.

F. Closed-Loop PID Controller

Linearising (10) about $\theta = 0$, with $u_c = DC - 0.5$ as the duty-cycle offset, gives the double-integrator plant $\ddot{y} = -2u_1^2\kappa\, u_c$. A PID control law, $u_{unsat} = -(K_p e + K_i \int e\, dt + K_d \dot{e})$, is saturated to $u_c \in [-0.5, 0.5]$, with gains chosen by matching the closed-loop characteristic polynomial to a triple pole at $-\omega_n$, i.e. $(s + \omega_n)^3$:

$$K_p = \frac{3\omega_n^2}{g}, \quad K_i = \frac{\omega_n^3}{g}, \quad K_d = \frac{3\omega_n}{g}, \quad g = 2u_1^2\kappa. \tag{14}$$

This controller is closed around the plant with a saturation-aware integral rule: whenever the actuator is already saturated in the direction the error is pushing it, the integral term stops accumulating. These gains, computed once from the constant nominal κ, are held fixed throughout every result in Section V, including for the beam-coupled plant, so that any change in performance is caused by the plant changing, not by quietly re-tuning the controller behind the scenes.

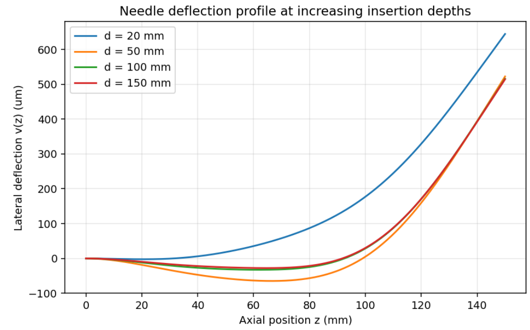

Fig. 5. Left: convergence of $v(L)$ with the number of retained modes N. Right: convergence of the full deflection-profile shape for $N = 1, 2, 4, 6$.

G. Modelling Assumptions

On the mechanics side, the beam uses small-deflection Euler-Bernoulli theory, reasonable for a thin steel shaft but not for a much softer or more curved needle. The tissue foundation is one uniform, linear-elastic material with stiffness K_e, ignoring layered, only-approximately-linear real tissue. The beam calculation is quasi-static, so dynamic or inertial shaft effects are ignored throughout, including in the beam-coupled loop, and the mode shapes $M_i(z)$ assume a base clamp that is exactly correct only at the start of insertion.

On the motion side, the tip is a nonholonomic, no-slip vehicle confined to one plane, so out-of-plane bending is not represented, and the duty-cycle averaging in (10)–(11) only holds because the bevel-flip period T is assumed much shorter than the insertion time.

On the control side, the PID gains in (14) come from a linearised, constant-κ plant and are applied unchanged to the full nonlinear, depth-varying plant in simulation; this is intentional, since Section IV-E is meant to show what a controller that does not know about the changing gain actually does. The calibration constant C in (13) is likewise fixed at one reference condition rather than fitted to data.

Finally, E, I, K_e, and Q are taken directly from [3] rather than measured independently. Every result has been checked against known limiting cases and modal convergence,

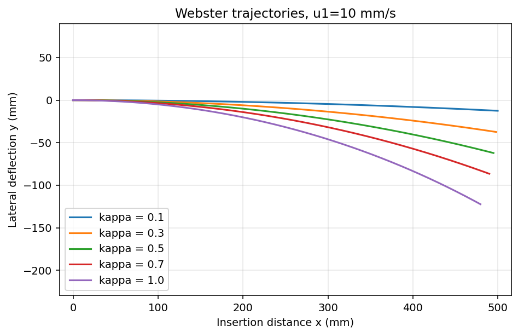

Fig. 6. Tool-tip trajectories at $u_1 = 10$ mm/s, $\kappa \in \{0.1, \ldots, 1.0\}$ m^{-1}.

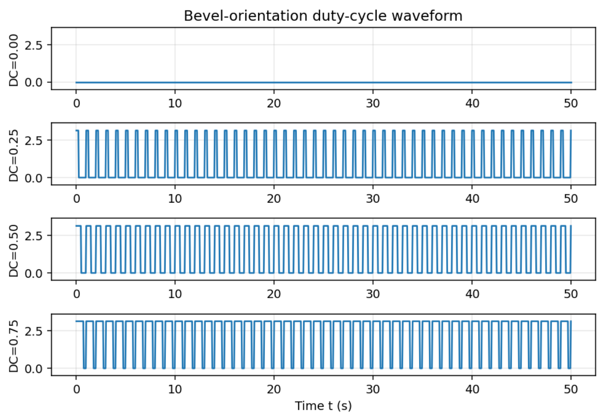

Fig. 7. Bevel-orientation waveform $\theta_{bevel}(t)$ at four duty cycles.

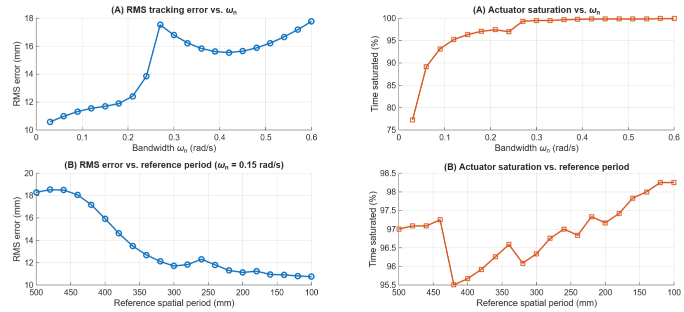

Fig. 8. (A) RMS error and saturation fraction vs. bandwidth ω_n. (B) The same, vs. reference period.

confirming the code matches the mathematics; Section VI discusses what this does, and does not, establish.

V. Simulation Results

Mode shapes and convergence. Fig. 2 and Table I confirm the expected nodal structure of the mode shapes and show that $N = 4$ modes are within 1.7% of the $N = 6$ result; Fig. 5 shows how the full deflection-profile shape converges as more modes are added, with tip deflection saturating at $\approx 515\,\mu$m beyond $d \approx 50$ mm.

Beam-coupled curvature. Table III shows the non-monotonic depth-dependence explained in Section IV-E, a behaviour completely absent from the purely kinematic model, which simply assumes a constant κ regardless of depth.

Trajectories and duty cycle. Figs. 6 and 7 confirm the expected monotonic relationship between κ and lateral drift, and confirm that the duty-cycle waveform behaves exactly as intended.

Bandwidth sweep. Fig. 8 sweeps two things: (A) controller bandwidth ω_n from 0.03 to 0.60 rad/s with a fixed 15 mm, 300 mm S-curve reference, and (B) the reference period from 500 mm down to 100 mm with a fixed $\omega_n = 0.15$ rad/s, both using the purely kinematic curvature law. In sweep (A), RMS tracking error is lowest, about 10.6 mm, at the smallest ω_n, rises to a peak of about 17.6 mm near $\omega_n = 0.27$, dips to about 15.5 mm near $\omega_n = 0.42$, and rises again, while the fraction of time the actuator spends saturated climbs from about 77% to nearly 100% by $\omega_n \approx 0.3$. In sweep (B), RMS error is largest, about 18.3 mm, at the longest reference period, where transient behaviour and phase lag dominate; it dips to about 11.7 mm near a 300 mm period, then falls toward a floor of about 10.7–10.8 mm as the period shortens further, close to the reference signal's own RMS value of $15/\sqrt{2} \approx 10.6$ mm. This coincides with the actuator being saturated for an increasing fraction of the insertion, so bandwidth alone is not a reliable predictor of tracking quality once saturation-limited.

Closed-loop control, kinematic vs. beam-coupled. Fig. 9 compares the purely kinematic curvature law (10) against the beam-coupled law of Section IV-E, using exactly the same fixed gains (14) with no re-tuning. In Mode A, regulation to -20 mm, the kinematic controller settles to about 2 mm of final error (10% of setpoint), while the beam-coupled controller settles to about 5.9 mm (30%), despite a slightly smaller overshoot (≈ -38 mm versus ≈ -40 mm). This is not a sign that the coupling is broken; it is the coupling doing exactly what it should. Table III and Fig. 9(A) show that the true plant gain varies by up to 65% over the depth range Mode A actually travels ($x \lesssim 40$ mm), and the fixed gains in (14), derived assuming constant κ, cannot track that variation. This is a direct, quantitative demonstration that a fixed-gain PID controller is not enough once the plant's true, mechanics-based gain changes with depth, and it is the strongest argument for the gain-scheduled controller proposed in Section VI. In Mode B, S-curve tracking, both curvature laws give an almost identical RMS error of about 12.0 mm, because the reference here mostly covers depths ($d \gtrsim 100$ mm) where $\kappa_{beam}(d)$ has already converged to within 1% of nominal.

VI. Discussion and Future Work

Each sub-model was checked on its own before combination, so mistakes could be traced to a single layer. Section IV-E wires the beam mechanics into the real-time loop; in an earlier, disconnected version it was validated alone but never drove the controller. This is progress in *internal consistency* but not *experimental validation*: every result in this paper comes from MATLAB simulation, and no anchor-case or convergence check substitutes for comparison against real

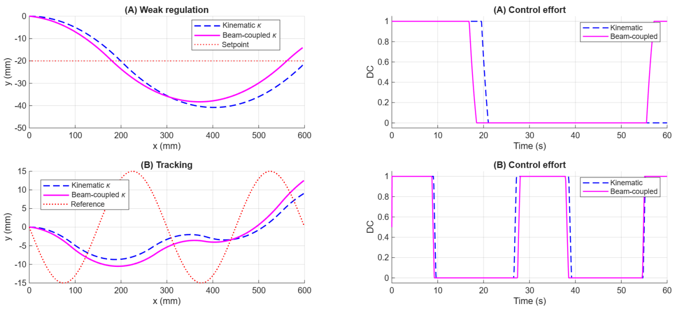

Fig. 9. Kinematic (dashed blue) vs. beam-coupled (solid magenta) curvature law, identical fixed gains. (A) Weak regulation and control effort. (B) S-curve tracking and control effort.

phantom or ex-vivo tissue; C in (13) remains a single, stress-tested assumption never fitted to data.

The value of this coupling is diagnostic rather than predictive. Table III and Fig. 9(A) show the fixed-gain controller of Section IV-F is measurably mismatched to the true, depth-varying plant gain, costing roughly a threefold drop in weak-regulation accuracy, a finding the sensitivity check in Section IV-E holds to be qualitatively solid even though its exact size depends on C. The obvious next step is a depth-scheduled controller recomputing (14) from the local $\kappa_{beam}(d)$ instead of one fixed nominal κ. The bandwidth sweep (Fig. 8) is similarly tied to actuator saturation; a cleaner sweep would hold the reference-cycle count fixed rather than total insertion distance, to isolate genuine bandwidth-limited behaviour from transients.

Closing the gap to experimental validation is the clearest priority ahead. Two recent studies point to low-cost routes: Zandonà et al. [10] identified kinematic model parameters directly from RGB-D-tracked insertions into silicone prostate phantoms of varying stiffness, at sub-millimetre accuracy, a realistic near-term route to fitting C and (K_e, Q) against real trajectories instead of borrowing them from [3]; Lehocky et al. [11] used a hyperelastic-viscoelastic finite-element tissue model showing needle-tip fillet radius dominates tissue stress and strain, and that slower insertion keeps strain rates lower, a useful safety cross-check for the duty-cycle rotation rates used here once ex-vivo testing is pursued.

Two further steps stand out: replacing the Winkler foundation with a Kelvin-Voigt element to let $\kappa_{beam}(d, u_1)$ depend on insertion speed, matching [3]'s observation that fitted tissue parameters vary with speed and capturing the relaxation [11] observed directly; and fitting C and (K_e, Q) to gelatine-phantom data as in [10] rather than borrowing them. More broadly, a low-cost, gain-scheduled version validated on gel phantoms and then ex-vivo tissue is a realistic target for bringing steerable-needle biopsy and regional anaesthesia to lower-resource settings, the long-term motivation behind this work.

VII. Conclusion

This paper reimplemented and numerically verified, in MATLAB, a four-part needle-steering pipeline built from established sub-models, connected by a beam-coupled curvature law linking beam mechanics directly to the real-time control loop. A Rayleigh-Ritz convergence study justified $N = 4$ modes, within 1.7% of $N = 6$. The coupling revealed a non-monotonic, depth-varying effective curvature, 65% above nominal near the surface and 10% below near $d = 20$ mm, and a threefold drop in fixed-gain weak-regulation accuracy; a sensitivity check showed this qualitatively robust even though its exact size depends on the calibration constant. A two-dimensional bandwidth sweep showed tracking error does not simply improve with bandwidth once the actuator saturates. Fitting the calibration constant to phantom data [10], cross-checking tissue safety limits [11], and building a depth-scheduled controller are the concrete next steps toward a pipeline fit for real tissue testing.

Acknowledgment

The author thanks the IEEE Robotics and Automation Society, OAU Student Chapter, for their support of this work, and is deeply grateful to his parents for their inspiration and continued support of his education.

References

[1] R. J. Webster III, J. S. Kim, N. J. Cowan, G. S. Chirikjian, and A. M. Okamura, "Nonholonomic modeling of needle steering," *Int. J. Robotics Research*, vol. 25, no. 5–6, pp. 509–525, 2006.
[2] S. Misra, K. B. Reed, B. W. Schafer, K. T. Ramesh, and A. M. Okamura, "Mechanics of flexible needles robotically steered through soft tissue," *Int. J. Robotics Research*, vol. 29, no. 13, pp. 1640–1660, 2010.
[3] R. J. Roesthuis, Y. R. J. van Veen, A. Jahya, and S. Misra, "Mechanics of needle-tissue interaction," in *Proc. IEEE/RSJ Int. Conf. Intelligent Robots and Systems (IROS)*, 2011, pp. 2557–2563.
[4] D. S. Minhas, J. A. Engh, M. M. Fenske, and C. N. Riviere, "Modeling of needle steering via duty-cycled spinning," in *Proc. 29th Annu. Int. Conf. IEEE Eng. Med. Biol. Soc. (EMBC)*, 2007, pp. 2756–2759.
[5] R. D. Blevins, *Formulas for Natural Frequency and Mode Shape*. New York, NY, USA: Van Nostrand Reinhold, 1979.
[6] S. P. Timoshenko, *Strength of Materials, Part I: Elementary Theory and Problems*, 3rd ed. New York, NY, USA: Van Nostrand, 1955.
[7] R. J. Roesthuis, M. Abayazid, and S. Misra, "Mechanics-based model for predicting in-plane needle deflection with multiple bends," in *Proc. 4th IEEE RAS EMBS Int. Conf. Biomedical Robotics and Biomechatronics (BioRob)*, 2012, pp. 69–74.
[8] M. Khadem, B. Fallahi, C. Rossa, R. S. Sloboda, N. Usmani, and M. Tavakoli, "A mechanics-based model for simulation and control of flexible needle insertion in soft tissue," in *Proc. IEEE Int. Conf. Robotics and Automation (ICRA)*, 2015, pp. 2264–2269.
[9] T. Adebar, A. E. Fletcher, and A. M. Okamura, "3-D ultrasound-guided robotic needle steering in biological tissue," *IEEE Trans. Biomed. Eng.*, vol. 61, no. 12, pp. 2899–2910, 2014.
[10] C. Zandonà, A. Roberti, D. Costanzi, B. Gül, Ö. Akbulut, P. Fiorini, and A. Calanca, "A comparison between kinematic models for robotic needle insertion with application into transperineal prostate biopsy," *Technologies*, vol. 12, no. 3, p. 33, 2024.
[11] C. A. Lehocky, Y. Shi, and C. N. Riviere, "Hyper- and viscoelastic modeling of needle and brain tissue interaction," in *Conf. Proc. IEEE Eng. Med. Biol. Soc.*, 2014, pp. 6530–6533.